Supporting Information

Enhancing the Quality Factors of Guided Resonances via Rational Symmetry Breaking

Shiwang Yu, Yuexin Sun, Duk-Yong Choi, Zhancheng Li, Wenwei Liu, Wenyuan Zhou, Hua Cheng*, and Shuqi Chen**

Dr. S. Yu, Dr. Y. Sun, Prof. Z. Li, Prof. W. Liu, Prof. W. Zhou, Prof. H. Cheng, Prof. S. Chen
The Key Laboratory of Weak Light Nonlinear Photonics, Ministry of Education, Ministry of Education, School of Physics and TEDA Institute of Applied Physics, Nankai University, Tianjin 300071, China
E-mail: zcli@nankai.edu.cn; hcheng@nankai.edu.cn; schen@nankai.edu.cn
Prof. D.-Y. Choi
Laser Physics and Centre, Research School of Physics, Australian National University, Canberra, ACT 2601, Australia
Prof. S. Chen
School of Materials Science and Engineering, Nankai University, Tianjin 300350, China
Prof. S. Chen
The Collaborative Innovation Center of Extreme Optics, Shanxi University, Taiyuan, Shanxi 030006, China

This file includes:

S1. Analysis on the radiation characteristics of Brillouin zone folding-induced guided resonances in the conventional Δ*g*-perturbed and Δ*S*-perturbed metasurfaces.

In diatomic metasurfaces, Brillouin zone folding-induced guided resonances can be realized not only by varying the spacing between adjacent nanostructures (Δ*g*-perturbed) but also by modulating their individual sizes (Δ*S*-perturbed). These two conventional methods have been discussed in detail in previous works[1]. As shown in Figure S1, the two methods each preserve one C_2 rotation center of the original unperturbed metasurface, the corresponding eigenmodes in the two perturbed metasurfaces manifest as opposite quasi-GMs or BICs. From the evolution of the *Q* factor in momentum space, it is evident that the Δ*S*-perturbed metasurfaces exhibit lower robustness compared with the Δ*g*-perturbed metasurfaces. Therefore, in the main text, we use only the Δ*g*-perturbed metasurfaces as an illustrative example for analysis.

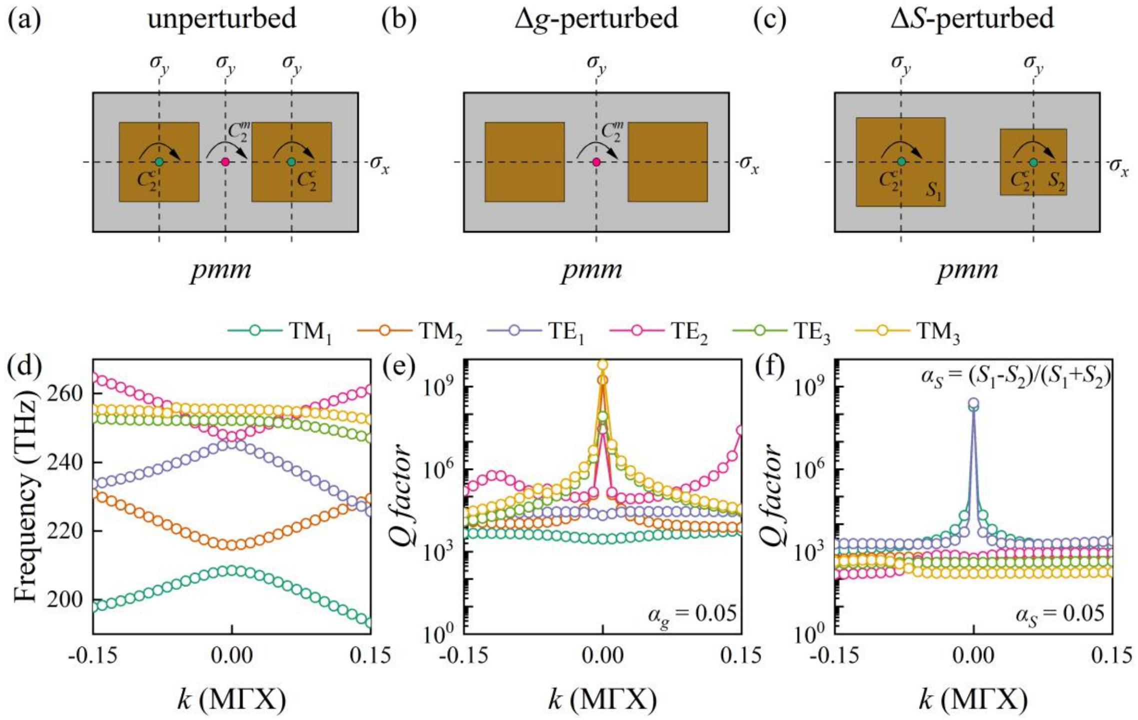

Figure S1. Symmetry operations for the rectangular lattices (point group: C_{2v}) of the (a) unperturbed, (b) conventional Δ*g*-perturbed, and (c) conventional Δ*S*-perturbed metasurfaces. (d) Calculated band diagram and *Q* factor distributions in momentum space of the (e) Δ*g*-perturbed and (f) Δ*S*-perturbed metasurfaces at $\alpha = 0.05$.

S2. Analysis on the radiation characteristics of the eigenmodes in the Δ*g*-perturbed and Δ*l*-perturbed metasurfaces

To more clearly and intuitively demonstrate that our design strategy enhances the *Q* factors of all guided resonances in the metasurface, we calculated the resonances within the zero-order diffraction domain as a function of the wave vector *k* and asymmetry factor *α*. These calculations, performed for the metasurface under two perturbations, are presented in Figure S2. For the quasi-GMs (TM$_1$-QGM and TE$_1$-QGM), as illustrated in Figure S2(a)-(d), the *Q* factor decreases gradually with increasing asymmetry factor (*α*), independent of the wave vector (*k*). However, when either *k* or *α* is held constant, the *Q* factors of our proposed Δ*l*-perturbed metasurface improve by more than an order of magnitude compared with those of the conventional Δ*g*-perturbed metasurface. For BICs, a similar enhancement in the *Q* factor is achieved, as demonstrated in Figure S2(e)-(h). Notably, the increase in *Q* values for the TE$_2$-BIC and TM$_3$-BIC eigenmodes at large wave vectors *k* arises from mode coupling and the emergence of the accidental BIC.

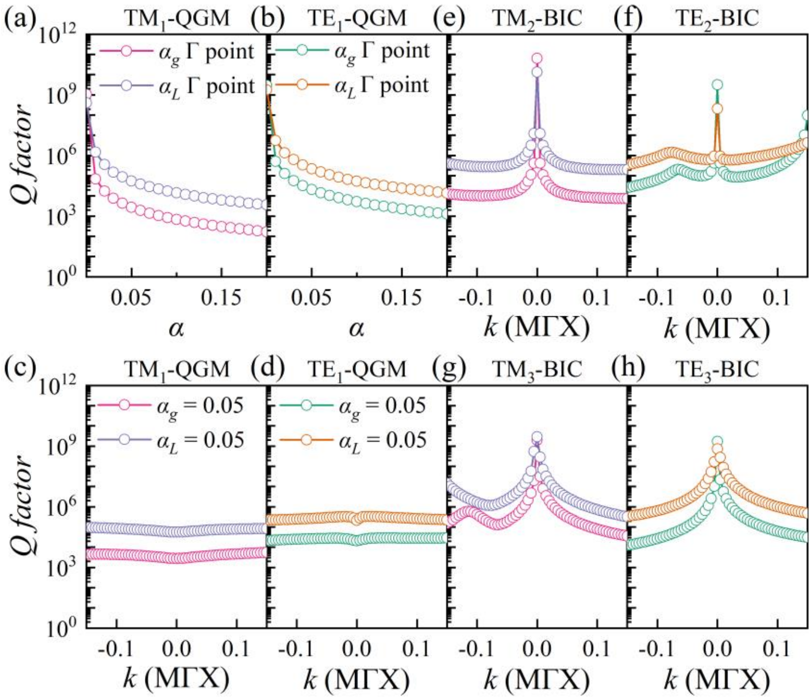

Figure S2. Calculated *Q* factor distribution as functions of the wavevector *k* or asymmetry factor *α* for six folded eigenmodes within the zero-order diffraction domain**.** (a) TM$_1$-QGM (b) TE$_1$-QGM modes at the Γ point and (c) TM$_1$-QGM (d) TE$_1$-QGM (e) TM$_2$-BIC (f) TE$_2$-BIC (g) TM$_3$-BIC (h) TE$_3$-BIC modes at $\alpha = 0.05$.

S3. Group symmetry analysis of the eigenmodes

To elucidate the mechanism behind the formation of quasi-GMs and BICs induced by band folding, we analyze the symmetries of the eigenstates before and after symmetry breaking by examining the in-plane symmetries of the out-of-plane field components.[1-4] From a group theory perspective, the symmetry of an eigenmode can be described using the irreducible representation associated with its characteristic table. For the metasurface under study, which belongs to the $C_{2\mathrm{v}}$ point group, the corresponding character table is presented in Table 1. Here, the values 1 and -1 represent the even and odd parity, respectively, of the eigenfield under specific symmetry operations: C_2, σ_y, and σ_x. Figure S3 illustrates the changes in the symmetry operations of the rectangular lattice before and after the perturbation, while Table 2 presents the irreducible representations of the various eigenstates within the unperturbed and symmetry-breaking metasurfaces.

Table 1. The character table for the $C_{2\mathrm{v}}$ point group

$C_{2\mathrm{v}}$	E	C_2	σ_y	σ_x
A_1	1	1	1	1
A_2	1	1	-1	-1
B_1	1	-1	1	-1
B_2	1	-1	-1	1

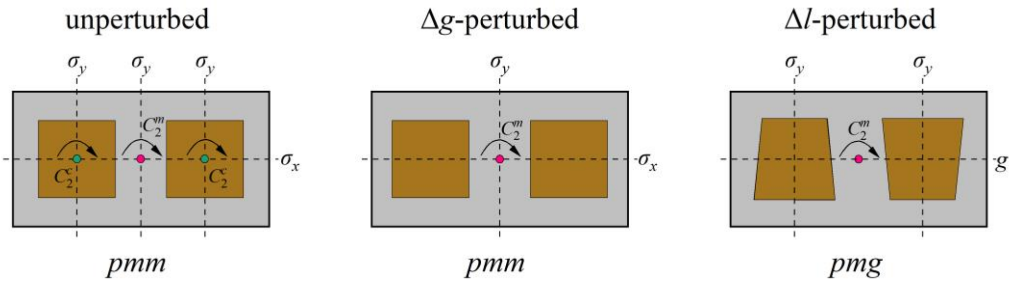

Figure S3. Symmetry operations for the rectangular lattices (point group: $C_{2\mathrm{v}}$) of the unperturbed, conventional Δg-perturbed, and our proposed Δl-perturbed metasurfaces. Here, C_2^m and C_2^c denote the C_2 rotation centers: C_2^m is located at the midpoint between two neighboring nanobricks, while C_2^c is at the center of a single nanobrick. σ_x and σ_y represent mirror operations in the x and y directions, respectively, and 'g' signifies the glide reflection operation.

Table 2. The irreducible representations of various eigenmodes in the unperturbed and perturbed metasurfaces

eigenmodes	unperturbed (*pmm*)	Δ*g*-perturbed (*pmm*)	Δ*l*-perturbed (*pmg*)
	C_2^m / C_2^c	C_2^m	C_2^m
$\mathrm{TM_1}$-QGM	B_2/A_1	B_2	B_2
$\mathrm{TM_2}$-BIC	A_1/B_2	A_1	A_1
$\mathrm{TE_1}$-QGM	B_2/A_1	B_2	B_2
$\mathrm{TE_2}$-BIC	$A_1/\ B_2$	A_1	A_1
$\mathrm{TE_3}$-BIC	A_2/B_1	A_2	A_2
$\mathrm{TM_3}$-BIC	A_2/B_1	A_2	A_2

S4. Calculation of the SHG conversion efficiency of hybrid silicon (Si)-lithium niobate (LN) metasurface

Since the near-field enhancement at resonance is linked to the radiative Q factor,[5] as shown in Figure 4(c) of the main text, our proposed Δl-perturbed metasurface can not only improve the Q values but also achieve significant near-field enhancement. As a result, we utilize strong resonant field enhancement to boost the nonlinear parametric process, such as the second harmonic generation (SHG).

Due to the large second-order nonlinear polarization coefficient of LN material, we constructed a Si-LN hybrid metasurface by adding a layer of LN beneath the Si dimer structure to enhance SHG conversion efficiency, as shown in Figure S4. The period along the x and y directions is $p_x = 810$ nm, and $p_y = 400$ nm, respectively. The Si thickness is $t_{Si} = 350$ nm, and the LN film thickness is $t_{LN} = 300$ nm. A 50 nm thick SiO_2 layer is added between the LN layer and the Si dimer structure to serve as an adhesive, preventing the structure from detaching. The entire sample is placed on a SiO_2 insulator substrate. The settings for the other structural parameters and the definition of the asymmetry factor are consistent with those in the main text. The optical axis of LN is oriented along the y-direction to maximize the utilization of its largest second-order nonlinear coefficient, d_{33}. Here, $d_{33} = -19.5$ pm/V and the anisotropic refractive indices of LN are $n_o = 2.21$ and $n_e = 2.14$.[6]

Figure S4(a) shows the calculated near-field enhancement at the resonant wavelength of the TE_1-QGM mode. It can be observed that our proposed Δl-perturbed metasurface exhibits reduced far-field radiation loss, with the y-direction electric field component E_y enhanced by nearly five times under the same asymmetry factor. Moreover, the electric field is primarily localized in the LN layer, which can be leveraged to enhance the nonlinear parametric process. We further calculated the forward SHG conversion efficiency at different wavelengths under a pump light intensity of $I_0 = 1$ [MW/cm^2], as illustrated in Figure S4(b) and (c). The results demonstrate that, compared to the conventional Δg-perturbed metasurface, the conversion efficiency η at the resonant wavelength exhibits a 500-fold enhancement. The calculated SHG output power as a function of pump power is shown in Figure S4(d) on a logarithmic scale. The fitting results demonstrate a quadratic dependence, confirming the generation of a SHG. Furthermore, when $\alpha_L = 0.6$ and the pump intensity $I_0 = 0.01$ [GW/cm^2], a high conversion efficiency of $\eta = 1.81\%$ is achieved at the resonant wavelength.

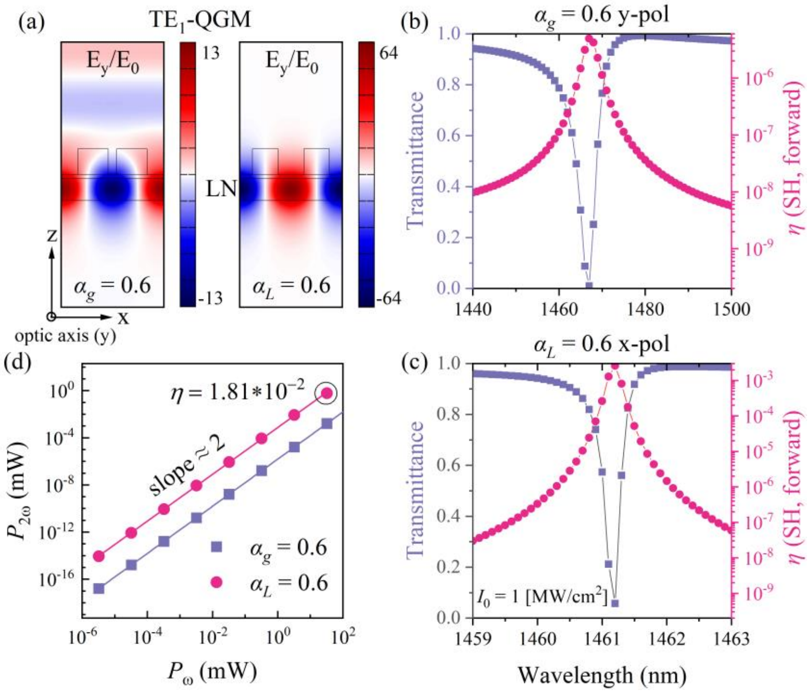

Figure S4. Calculated enhanced SHG conversion efficiency based on the symmetry-breaking metasurfaces perturbed by Δg and Δl. (a) Calculated modal electric field profile E_y of the TE$_1$-QGM mode supported by the Δg-perturbed (α_g = 0.6, left panel) and Δl-perturbed (α_L = 0.6, right panel) metasurfaces. The optical axis of LN is oriented along the y-direction. The calculated transmission spectrum at normal incidence and forward SHG conversion efficiency (η) at various pump wavelengths are presented for (b) α_g = 0.6 and (c) α_L = 0.6 when the pump intensity I_0 = 1 [MW/cm^2]. Here, η is defined as $\eta = P_{2\omega}/P_\omega$, where $P_{2\omega}$ represents the SHG output power, and P_ω denotes the pump power at the fundamental wavelength. (d) The calculated SHG power as a function of input pump power when asymmetry factor α = 0.6 is plotted in log-log coordinates. The solid line represents a quadratic fit.

S5. Multipole analysis expression for coupling amplitude calculation

The individual components of electric dipole moments (***p***), magnetic dipole moments (***m***), and electric quadrupole moments (***Q***) are as follows:[7]

$$p_\alpha = \frac{1}{i\omega}\int_V J_\alpha dV,$$

$$m_\alpha = \frac{1}{2c}\int_V [r \times J]_\alpha dV,$$

$$Q_{\alpha,\beta} = \frac{1}{2i\omega}\int_V [r_\alpha J_\beta + r_\beta J_\alpha - \frac{2}{3}\delta_{\alpha,\beta}(\boldsymbol{r}\cdot\boldsymbol{J})].$$

Here, α, β = x, y, z *and* $J_\alpha = i\omega\varepsilon_0(\varepsilon_r - 1)E_\alpha$ respresent the displacement current density. ω denotes the angular frequency, ε_0 represents the permittivity in vacuum, ε_r is complex relative permittivity. For the simulation results presented in Figures 1–4 of the main text, the α-Si scatterers were assumed to be embedded in a uniform air background. Accordingly, the integration region V excluded the substrate, and the coordinate origin was set at the geometric center of the scatterer. Since the simulation preserves the out-of-plane mirror symmetry of the metasurface, the mesh size and the selection of the integration region affect only the numerical values of the multipole moments, without altering their evolution under different asymmetry factors. To characterize numerical uncertainties in the calculated coupling amplitudes, we expanded the integration volume along the z-direction in discrete steps. The multipole moment coefficients were then calculated in three different integration regions (either a Si structure alone or a Si structure combined with two different air-layer thicknesses), and the corresponding means and uncertainties were obtained, as indicated by the error bars in Figures 4(d) and 4(e) of the main text. For both types of metasurfaces, the same mesh was used to ensure a valid comparison of the calculated Q factors.

S6. Experimental setup and Fano formula fitting

The experimental setup used for spectrum measurements is shown in Figure S5. The measured transmittance spectrum can be described by the Fano formula:[8-10] $T(\omega) = T_0 + A_0 \frac{[q + 2(\omega - \omega_0)\Lambda]^2}{1 + [2(\omega - \omega_0)\Lambda]^2}$. Here, q is the Fano asymmetry parameter, ω_0 is the resonance frequency, Λ is the resonance linewidth. T_0 and A_0 describe the background contribution of non-resonant modes to the resonant peak amplitude and the offset, respectively. The Q factors can be obtained by $Q = \frac{\omega_0}{\Lambda}$. The specific fitting results of the experimental transmission spectra are shown in Figure S6.

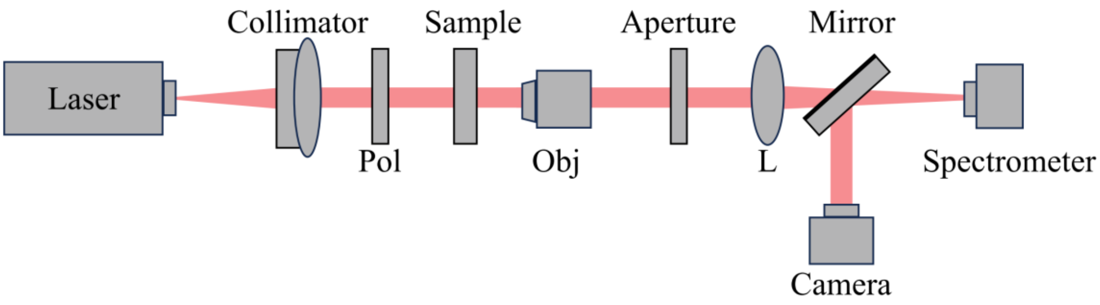

Figure S5. Schematic of the experimental setup used for transmission spectrum measurements. Pol: linear polarizer, Obj: objective lens, L: lens.

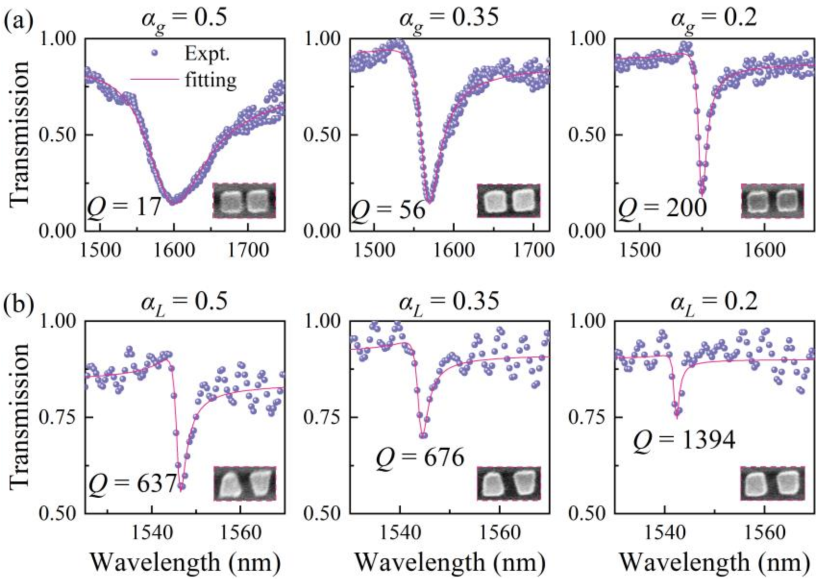

Figure S6. Fano formula fitting results for the experimental transmission spectra with varying asymmetry factors α_g and α_L. The bottom right insets represent the sample SEM images of the unit cell.

S7. The generalizability of the proposed symmetrical design strategy

The robustness of the *Q* factor can also be observed when the perturbed metasurface preserves the same *pmg* space group symmetry and selection rule[2]. In practical sample fabrication, modifying the shape of the geometric structure is more challenging than adjusting the relative positions of the structures. As shown in Figure S7, the Δ*y*-perturbed metasurface is achieved by altering the relative displacement of the two nanostructures within the unit cell along the *y*-direction, rather than varying the shape of the nanostructures through the Δ*l*-perturbed method. Both methods preserve the same *pmg* space group symmetry and selection rule for the eigenstates, and thus their eigenmodes exhibit similar scaling characteristics. As shown in Figures S7(e) and S7(f), under the same structural displacement ($\delta x = \delta y = 4.5$ nm), our design increases the *Q* factor in momentum space by more than two orders of magnitude compared with the conventional Δ*g*-perturbed metasurface. Therefore, based on our proposed symmetry design strategy, a higher *Q* factor can be achieved without altering the geometric dimensions of the structures.

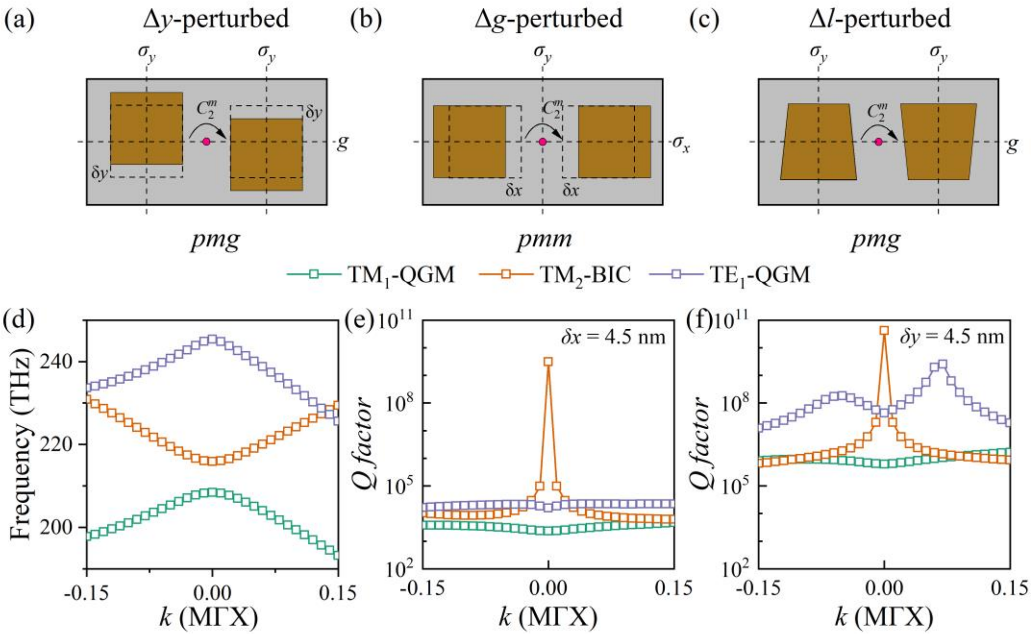

Figure S7. Symmetry operations for the rectangular lattices (point group: C_{2v}) of the (a) Δ*y*-perturbed, (b) conventional Δ*g*-perturbed, and (c) Δ*l*-perturbed metasurfaces. Here, δx and δy represent the offsets of two nanobricks from their original positions in the *x* and *y* directions. (d) Calculated band diagram and *Q* factor distributions in momentum space of the (e) Δ*g*-perturbed and (f) Δ*y*-perturbed metasurfaces.

References

[1] W. Wang, Y. K. Srivastava, T. C. Tan, Z. Wang, R. Singh, Brillouin zone folding driven bound states in the continuum. *Nat. Commun.* **2023**, 14, 2811.

[2] A. C. Overvig, S. C. Malek, M. J. Carter, S. Shrestha, N. Yu, Selection rules for quasibound states in the continuum. *Phys. Rev. B* **2020**, 102, 035434.

[3] K. Sakoda, Optical properties of photonic crystals (Springer Science & Business Media, Berlin, 2004).

[4] G. Xu, Z. Xue, J. Fan, D. Lu, H. Xing, P. P. Shum, Y. Zhou, L. Cong, Flexible Terahertz Metasurface Absorbers Empowered by Bound States in the Continuum *Adv. Mater.* **2024**, 36, 2470321.

[5] R. Chai, W. Liu, Z. Li, Y. Zhang, H. Wang, H. Cheng, J. Tian, S. Chen, Spatial Information Lasing Enabled by Full-k-Space Bound States in the Continuum. *Phys. Rev. Lett.* **2024**, 132, 183801.

[6] A. Fedotova, M. Younesi, J. Sautter, A. Vaskin, F. J. F. Löchner, M. Steinert, R. Geiss, T. Pertsch, I. Staude, F. Setzpfandt, Second-Harmonic Generation in Resonant Nonlinear Metasurfaces Based on Lithium Niobate. *Nano Lett.* **2020**, 20, 8608.

[7] P. C. Wu, C. Y. Liao, V. Savinov, T. L. Chung, W. T. Chen, Y.-W. Huang, P. R. Wu, Y.-H. Chen, A.-Q. Liu, N. I. Zheludev, D. P. Tsai, Optical Anapole Metamaterial. *ACS Nano* **2018**, 12, 1920.

[8] M. F. Limonov, M. V. Rybin, A. N. Poddubny, Y. S. Kivshar, Fano resonances in photonics. *Nat. Photonics* **2017**, 11, 543.

[9] K. Koshelev, S. Lepeshov, M. Liu, A. Bogdanov, Y. Kivshar, Asymmetric Metasurfaces with High-Q Resonances Governed by Bound States in the Continuum. *Phys. Rev. Lett.* **2018**, 121, 193903.

[10] S. You, H. He, Y. Zhang, H. Duan, L. Wang, Y. Wang, S. Luo, C. Zhou, Resonance Wavelength Stabilization of Quasi-Bound States in the Continuum Constructed by Symmetry Breaking and Area Compensation. *Nano Lett.* **2024**, 24, 15300.